Surface Cracking in Elastic-Plastic Multi-Layered Media Due to Repeated Sliding Contact

Z.-Q. Gong, Graduate Student
K. Komvopoulos, Professor, Fellow ASME

Department of Mechanical Engineering
University of California
Berkeley, CA 94720

Abstract

Surface cracking in a multi-layered medium due to sliding of a rigid asperity was analyzed using linear elastic fracture mechanics and the finite element method. Overlapping of the crack faces and assumptions about the distributions of surface tractions were avoided by using special contact elements. The main objectives of this study were to obtain solutions for the tensile and shear stress intensity factor (SIF) and to determine the crack propagation path in the first layer due to repetitive sliding. The crack propagation direction was predicted based on the maximum (tensile or shear) SIF range. The effects of crack length, sliding friction, and crack-face friction on the SIF and crack propagation direction are discussed in the context of finite element solutions. Simulation results demonstrate the effects of crack growth in the elastic surface layer on the accumulation of plastic strain in the elastic-plastic underlying layer and the significance of crack growth increment on the propagation path. It is shown that the surface crack propagates toward the layer interface at an angle of ~57 deg. from the original crack plane, independent of crack growth increment, in fair agreement with experimental observations. Based on the obtained results, a general fatigue approach for surface cracking is derived for multi-layered media subjected to repetitive sliding contact.

1. Introduction

Coatings are often used to enhance the tribological performance and endurance of various components with contact interfaces. The wear resistance of hard protective coatings, such as ceramics, cemented carbides, and diamond-like carbon, greatly affects the reliability of many mechanical systems. However, the inherent high hardness of these materials is obtained at the expense of low fracture toughness. Consequently, contact fatigue and/or fracture of hard overcoats are dominant failure mechanisms in many mechanical systems subjected to continuous sliding contact, such as gear flanks, bearing surfaces, and hard disk drives.

Contact analysis of layered media subjected to normal and tangential (friction) surface tractions has been the objective of numerous past studies. King and O'Sulllivan [1] investigated the plane-strain problem of a rigid cylinder sliding over an elastic layered half-space in both in-plane and anti-plane (i.e., along the cylinder axis) directions and found a high tensile stress at the trailing edge of the contact region. Kral and Komvopoulos [2] performed three-dimensional finite element simulations of a rigid spherical indenter sliding against an elastic-plastic layered medium and discussed the likelihood of transverse (ring) crack formation at the surface in the wake of the indenter. Ring crack formation has been observed on glass along the wake of a sliding conical indenter [3] and on the surface of carbon-coated magnetic rigid disks subjected to microscratching [4]. Gong and Komvopoulos [5] used the finite element method to analyze normal and sliding contact of a rigid cylindrical asperity on a patterned elastic-plastic layered medium. The high surface tensile stress at the trailing edge of the contact region indicated a greater probability of surface cracking in patterned layered media compared to smooth-surface media. In a three-dimensional thermomechanical analysis of Gong and Komvopoulos [6], a high thermal tensile stress was predicted slightly below the trailing edge of the contact region, which

is considered to be responsible for the initiation of thermal cracking in the wake of sliding microcontacts.

Although the contact stress/strain field in layered media has been extensively investigated, fracture mechanics studies are relatively sparse and limited to homogenous and brittle (elastic) half-spaces. Several fracture analyses of homogenous media [7-10] have shown that crack initiation is favored at the trailing edge of the contact region, where the maximum tensile stress arises during sliding. Beuth and Klingbeil [11] performed a plane-strain fracture analysis of an elastic thin film bonded to an elastic-plastic substrate and observed that substrate yielding increased the likelihood of film cracking due to the increase of the energy for crack growth in the film. Oliveira and Bower [12] studied fracture and delamination of thin coatings due to contact loading and reported a greater probability for fracture originating from flaws in the coating than the substrate or the interface. It was also found that the fracture load and crack pattern were strongly affected by the elastic property mismatch between the layer and the substrate materials.

Surface crack growth due to repeated sliding contact resembles a fatigue process in which the crack propagation rate is proportional to a power of the stress intensity factor (SIF) range, ΔK. Experiments by Mageed and Pandey [13] have shown that the crack propagation direction due to mixed mode cyclic loading can be determined from the maximum tensile stress criterion, which depends on ΔK_I and ΔK_{II}. Alfredsson and Olsson [14] performed experimental and numerical studies of normal contact fatigue caused by the formation of ring/cone and lateral cracks and discovered that surface crack growth occurred in the direction where the shear SIF was close to zero and that the propagation rate was dominated by ΔK_I. Lin and Smith [15,16] conducted a finite element fatigue analysis of surface cracked plates and obtained results for the SIF and fatigue life. Ko et al. [17] studied both experimentally and analytically crack growth and wear

particle formation on sliding steel surfaces and reported that the analytical predictions for the wear particle size and wear volume were in fair agreement with experimental results.

Despite valuable insight into surface cracking in thin coatings obtained from earlier studies, very little is known about the effect of plastic deformation in the underlying material (layer or substrate) on the growth direction of surface cracks. In addition, the effects of friction, initial crack length, and crack growth on the accumulation of plasticity in the underlying medium have not been considered in previous fracture mechanics analyses. Therefore, the objective of this investigation was to analyze surface cracking in a multi-layered medium due to repetitive sliding of a rigid asperity using the finite element method. SIF and crack propagation results are presented in terms of coefficient of friction at the contact region and crack interface and initial crack length. Another goal of this study was to develop a fracture mechanics approach that yields estimates of contact fatigue life for elastic-plastic multi-layered media undergoing surface cracking due to repetitive sliding contact.

2. Modeling Procedures

2.1 Problem Definition and Finite Element Model

Normal and shear tractions produced between contacting rough surfaces are transmitted through asperity microcontacts with statistical distributions depending on the effective surface roughness, normal load, and material properties of the interacting surfaces. When the average asperity spacing is significantly larger than the mean microcontact size, interaction of the stress/strain fields of neighboring microcontacts is secondary [18] and the problem is simplified to that of a single asperity in contact with a layered medium. Figure 1 shows schematically an asperity sliding over a layered medium containing a crack of initial length c_i perpendicular to the

free surface of the medium. The position of the asperity relative to the crack is denoted by y_P (Fig. 1).

Plane-strain sliding simulations were performed with a two-dimensional finite element mesh, such as that shown in Fig. 2(a), consisting of approximately 9,000 eight-node, isoparametric, quadrilateral elements (depending on the initial crack length and crack propagation path). The horizontal and vertical dimensions of the mesh are equal to $2.4R$ and $3.1R$, respectively, where R is the radius of the rigid asperity (assumed constant in all simulations). The nodes at the bottom boundary of the mesh were constrained against displacement in the vertical direction, while the nodes at the left boundary were constraint against displacement in the horizontal direction. The mesh was refined at the surface in order to increase the accuracy in the calculation of the contact area and stress/strain field in the highly stressed surface layer. The mesh was further refined around the crack, as shown in Fig. 2(b) for a propagating crack. In the vicinity of the crack tip, the mesh consists of 36 eight-node, isoparametric, collapsed quadrilateral plane-strain elements with their midside nodes adjacent to the crack tip displaced to the quarter-point distance in order to simulate the square root singularity of the stress field at the crack tip [19,20]. Since the analysis is based on linear fracture mechanics, the crack-tip nodes were constrained to move together in order to prevent crack-tip blunting during crack growth.

Special contact elements were used to model contact or separation between surface nodal points and the surface of the rigid asperity, based on the measurement of the relative distance of the two surfaces in the normal direction. If the obtained distance was less than the specified tolerance, it was assumed that contact was established and the appropriate contact force was applied at the corresponding node. The local surface overclosure (i.e., displacement of a nodal point at the surface of the deformable medium into the rigid surface) and relative slip were

obtained at each integration point of the contact elements. These kinematics were used in conjunction with appropriate Lagrange multiplier techniques to model surface interaction.

To examine the accuracy of the finite element model, especially the mesh around the crack tip, the classical problem of an edge-cracked medium subjected to far-field tension in the direction perpendicular to the crack plane was solved using the finite element mesh shown in Fig. 2. The entire mesh was modeled as a homogeneous elastic material. The value of the mode I SIF obtained from the finite element analysis was found to differ from the analytical solution [21] by only 2.3 percent, indicating the suitability of the finite element model for fracture analysis.

2.2 Material Properties and Plasticity Models

The thickness, h, elastic modulus, E, and yield strength, s_Y, of each layer in the multi-layered medium are given in Table 1. These thickness and mechanical property values are typical of layers used in magnetic rigid disks consisting of carbon overcoat (layer 1), CoCrPt magnetic medium (layer 2), CrV underlayer (layer 3), and NiP (layer 4) electroplated on Al-Mg substrate. The von Mises yield criterion was used to determine whether yielding occurred at a material point. The Mises yield condition, g, is expressed as

$$g = J_2 - k^2 = 0, \tag{1}$$

where k is a material constant, and J_2 is the second deviatoric stress invariant given by

$$J_2 = \frac{1}{2} S_{ij} S_{ij}, \tag{2}$$

where $S_{ij} = s_{ij} - d_{ij} s_m$, in which s_{ij} is the stress tensor, d_{ij} is Kronecker's delta function, and s_m is the mean octahedral stress ($s_m = s_{ii}/3$).

For uniaxial stress state, the yield criterion can be written as

$$s_M = \left[\frac{3}{2} S_{ij} S_{ij}\right]^{1/2} = s_Y, \tag{3}$$

where s_M is the von Mises equivalent stress, and s_Y is the yield strength under uniaxial tension. Plastic deformation was based on the usual associated flow rule, assuming negligible plastic volume change. An updated Lagrangian formulation was used in all contact simulations. In the present model, the first layer was assumed to be elastic, while all the other layers were modeled as elastic-perfectly plastic. The equivalent plastic strain, $\bar{e}_p$, is obtained as

$$\bar{e}_p = \int_\Omega [\frac{2}{3} de_{ij}^p de_{ij}^p]^{1/2}, \tag{4}$$

where W is the strain path, and e_{ij}^p denotes the components of the plastic strain tensor. The plastic flow rule was applied only to yielding material for which $s_M = s_Y$. The usual elastic constitutive equations were used when $s_M < s_Y$.

2.3 Calculation of Stress Intensity Factors

In linear elastic fracture mechanics, the normal and shear stresses at the crack tip due to sliding contact can be expressed in terms of the tensile (mode I) and shear (mode II) SIFs, K_I and K_{II} , respectively, defined as

$$K_I = \lim_{r \to 0} \sqrt{2pr}\, s_{yy}(r, q) \tag{5}$$

$$K_{II} = \lim_{r \to 0} \sqrt{2pr}\, t_{xy}(r, q), \tag{6}$$

where r and q are cylindrical polar coordinates and x and y are Cartesian coordinates at the crack tip (Fig. 1). Based on the method proposed by Chan et al. [22], the magnitudes of K_I and K_{II} were determined from linear extrapolation of least-square line fits to the s_{yy} and t_{xy} stress data calculated at ten nodes in the vicinity of the crack tip along the crack plane ($q = 0$). The

accuracy of this method has been evaluated in an earlier finite element analysis of Komvopoulos and Cho [23] dealing with subsurface crack propagation in a half-space due to a moving asperity.

2.4 Crack Growth Rate and Fatigue Life

The crack growth rate was assumed to follow a power-law relationship [24]

$$\frac{dc}{dN} = A(\Delta K)^m, \tag{7}$$

where N is the number of loading cycles (representing the number of asperity passes required for the crack to propagate by an infinitesimal distance, dc), and A and m are material constants.

Integration of Eq. (7) yields a fatigue life relation,

$$\int_0^{N_f} dN = \int_{c_i}^{c_f} \frac{dc}{A(\Delta K)^m}, \tag{8}$$

where N_f is the number of fatigue cycles required for the crack to grow from an initial length c_i to a length c_f. Since ΔK depends on the specific geometry, external loading, and crack length, it is not possible to obtain accurate estimates of fatigue life using Eq. (8). To circumvent this difficulty, an Euler integration algorithm was adopted in the numerical simulations,

$$N_{j+1} = N_j + \frac{\Delta c}{A\left[\Delta K(c_j)\right]^m} \qquad j = 0,1,\cdots,r \tag{9}$$

and

$$c_{j+1} = c_j + \Delta c \ , \tag{10}$$

where c_j is the crack length in the jth crack growth cycle, and Δc is the crack growth increment, which is constant in each simulation. The effect of the crack growth increment on the crack propagation path is discussed in a later section.

2.5 Simulation of Sliding Contact and Crack Growth

Simulations were performed with the finite element code ABAQUS (version 5.8). Each simulation consisted of three sequential steps. First, the rigid asperity was incrementally advanced into the medium to a specified depth and then displaced tangentially over the neighborhood of the surface crack by a distance approximately equal to eight times the half-contact width. Finally, the asperity was unloaded following the same incremental path as for the loading. These simulation steps were repeated in the same order for several cycles in order to model repetitive sliding. To examine the dependence of the SIFs on friction, the coefficient of friction between the surface of the multi-layered medium and the asperity, m, and the crack faces, m_c, was varied between 0 and 0.5. In order to study the effect of the initial crack length on the SIF distributions and crack propagation direction, four initial crack lengths (i.e., c_i/h_1= 0.125, 0.25, 0.5, and 0.875) were used in the finite element model. After each loading cycle, the mesh around the crack tip was modified to account for the growth of the crack by the specified increment in the direction of maximum tensile SIF range, $\Delta K_s^{\max}$, determined during the particular loading cycle.

To account for the deformation history effect on the SIF ranges, crack propagation, and evolution of plasticity in the second layer, the stress/strain state in the multi-layered medium generated after a given number of cycles was included in the subsequent loading cycle by using the following method. First, sliding of the asperity over the modified mesh was simulated with all the nodes of the kink faces locked together. Then, the nodes of the first kink were unlocked and asperity sliding over the medium was simulated again following exactly the same path. This procedure was repeated until all the kinks were unlocked sequentially. Finally, a new crack growth increment was simulated in the next sliding cycle. In view of the excessive computational

time of these crack growth simulations, only one initial crack length (c_i/h_1 = 0.25), but different crack growth increments, were modeled in this study. A simulation was terminated when the crack propagated very close to the interface of the first and second layers.

3. Results and Discussion

3.1 Crack Length Effect

To obtain generalized solutions, the SIFs were normalized by $2P/\pi a^{1/2}$, where P is the normal force applied by the moving asperity, and a is the corresponding half-contact width. In addition, the asperity distance from the crack, y_P, was normalized by the half-contact width, and the crack length by the thickness of the first layer, h_1. Figure 3(a) shows K_I as a function of dimensionless asperity position and crack length for $m = m_c = 0.5$. In all simulation cases, K_I assumes nonzero values only when the asperity passes over the crack ($y_P/a > 0$), apparently due to the effect of crack closure that is enhanced by the predominantly compressive stress field ahead of the sliding asperity. When the crack is just behind the trailing contact edge ($y_P/a > 1$), K_I increases rapidly to a peak value and then decreases gradually as the asperity moves further to the right of the crack. In addition, Fig. 3(a) reveals a strong dependence of K_I on crack length, indicating that the longer the crack, the higher the tensile stress at the crack tip. Moreover, the maximum K_I increases with an increase in crack length and the corresponding asperity position occurs further to the right of the crack.

The variation of K_{II} with asperity position and initial crack length, shown in Fig. 3(b), is complex compared to that of K_I. The range of K_{II} increases with crack length; however, K_{II} decreases rapidly to zero after the asperity passes over the crack ($y_P/a > 1$). When the asperity slides over the crack region, the predominant mode changes from shear to tensile. However, a

comparison of the results shown in Figs. 3(a) and 3(b) shows that ΔK_{II} is significantly less than ΔK_I, approximately by an order of magnitude. Hence, because the crack growth rate depends on ΔK (Eq. (7)), it may be inferred that crack growth is predominantly affected by the tensile mode.

3.2 Sliding Friction Effect

The stress field in the vicinity of the crack tip is strongly affected by the magnitude of friction traction at the surface. Figure 4 shows the variation of K_I and K_{II} with asperity position and coefficient of friction at the contact region ($m = 0.1$, 0.25, and 0.5) for $c_i/h_1 = 0.125$ and $m_c = 0$. The increase of K_I and K_{II} with friction coefficient is a consequence of the enhancement of the shear traction at the contact region and the higher stresses produced at the crack tip. The maximum value of K_I occurs as soon as the asperity slides over the crack, while that of K_{II} occurs when the asperity is over the crack.

Figures 5 shows the effect of coefficient of friction between the crack faces on the variation of K_I and K_{II} for $c_i/h_1 = 0.125$ and $m = 0.5$. Figure 5(a) shows that K_I is not affected by the friction condition at the crack interface. This is expected because the magnitude of K_I is controlled solely by the s_{yy} stress (Eq. (5)), which is not affected by the shear traction generated between the crack faces. Although the variation of K_{II} with asperity position is qualitatively similar to that shown in Fig. 4(b), K_{II} deceases with the increase of crack-face friction, which is opposite from the trend obtained with the increase of coefficient of friction at the contact interface. This behavior is attributed to reduced slip between the crack faces due to the increase of the coefficient of friction at the crack interface. Thus, crack-face friction promotes shear stress relaxation, in agreement with the fracture mechanics analysis of Komvopoulos and Cho [23] for subsurface crack growth parallel to the free surface of a homogeneous half-space. Since K_I is

significantly greater than K_{II} (Figs. 4 and 5), it may be inferred that sliding friction exhibits a strong effect on the variation of the tensile and shear SIFs, whereas the effect of crack-face friction is relatively secondary.

3.3 Crack Growth Direction

The crack growth direction was determined based on the maximum shear or tensile SIF ranges. The dominance of the shear and tensile modes during crack growth depends on the maximum values of ΔK_s and ΔK_t, where K_s and K_t are given by [25]

$$K_\sigma(\theta, y_P/a) = \sigma_\theta \sqrt{2\pi r} = \cos\frac{\theta}{2}\left[K_I \cos^2\frac{\theta}{2} - \frac{3}{2}K_{II}\sin\theta\right] \tag{11}$$

$$K_\tau(\theta, y_P/a) = \sigma_{r\theta} \sqrt{2\pi r} = \cos\frac{\theta}{2}\left[K_I \sin\theta + K_{II}(3\cos\theta - 1)\right] \tag{12}$$

Because of the dependence of K_I and K_{II} on asperity position (Figs. 3-5), K_s and K_t are functions of y_P/a. The maximum tensile and shear SIF ranges, $\Delta K_s^{\max}$ and $\Delta K_t^{\max}$, respectively, are defined as

$$\Delta K_s^{\max} = \max[\Delta K_s(q)] = \max[K_{s,\max}\big|_{q=q^*} - K_{s,\min}\big|_{q=q^*}] \tag{13}$$

$$\Delta K_t^{\max} = \max[\Delta K_t(q)] = \max[K_{t,\max}\big|_{q=q^*} - K_{t,\min}\big|_{q=q^*}] \tag{14}$$

where subscripts max and min denote maximum and minimum values of K_s and K_t, and q^* is a given value of q, which varies between –180 and 180 deg. For fixed angle $q = q^*$, $K_{\sigma,\max}\big|_{\theta=\theta^*}$ and $K_{\sigma,\min}\big|_{\theta=\theta^*}$ were determined at different asperity positions during a sliding cycle. Then, the angle q was varied between -180 and 180 deg. to determine the maximum value of $(K_{\sigma,\max}\big|_{\theta=\theta^*} - K_{\sigma,\min}\big|_{\theta=\theta^*})$, which is used to obtain $\Delta K_\sigma^{\max}$. The same procedure was used to

determine $\Delta K_t^{\max}$. Based on this approach, the crack growth direction was determined from Eqs. (11)-(14).

Figure 6 shows the variation of dimensionless ΔK_s and ΔK_t with angle q and crack length for $m = m_c = 0.5$. The increase of ΔK_s and ΔK_t with crack length is a consequence of the increase of K_I with crack length and the relatively small contribution of K_{II} (Fig. 3). The fact that the maximum values of ΔK_s are higher than those of ΔK_t indicates the dominance of the tensile mode in the crack growth process. Moreover, the maximum values of ΔK_s occur at an angle $q \approx 10$ deg. independent of crack length, suggesting that crack propagation will occur toward the sliding direction. Figure 7 shows the initial crack propagation direction, i.e., first deviation (kink) angle, q_1, as a function of initial crack length for $m = m_c = 0.5$. The data indicate a greater tendency for shorter cracks to propagate initially toward the sliding direction than longer cracks.

3.4 Crack Propagation

To examine the evolution of crack-tip stresses, development of crack growth path, and accumulation of plastic deformation in the underlying layer, results are presented in this section for $c_i/h_1 = 0.25$ and $m = m_c = 0.5$. Crack propagation was simulated based on the crack growth direction predicted based on the maximum tensile SIF range, assuming a certain crack growth increment. As explained in section 2.5, the stress and strain fields produced in a given crack growth cycle were updated in the subsequent cycle in order to simulate continuous crack growth by taking into account the stress/strain history effect.

Figure 8 shows the effect of crack growth cycles on the variation of dimensionless K_I and K_{II} with dimensionless asperity position for $\Delta c = h_1/8$. In each cycle, the crack propagated by

an increment Δc in the direction of $\Delta K_s^{\max}$. Figure 8(a) shows that the variation of K_I with asperity position is qualitatively similar to that shown in Fig. 3(a). However, crack growth causes the increment of ΔK_I initially to increase and then to exhibit small fluctuations with further crack growth, which are attributed to variations in the crack growth direction as the crack propagates deeper into the first layer, discussed in detail below. In addition, crack growth produces nonzero K_I values even when the asperity is to the left of the crack and causes the maximum value of ΔK_I to occur at a greater distance of the asperity from the crack. These phenomena are attributed to the effect of crack face separation (either partial or complete) and the mixed mode crack growth. As discussed earlier, the appreciably lower values of K_{II}, by an order of magnitude, compared to those of K_I (Fig. 8(b)) reveal a dominant effect of the tensile mode in crack propagation. Indeed, in all crack growth cycles it was found that $\Delta K_s^{\max} > \Delta K_t^{\max}$. Table 2 gives normalized $\Delta K_\sigma^{\max}$ in terms of deviation angle at each crack growth cycle, Δq, total deviation angle from the initial crack direction (perpendicular to the surface), q_{total}, and corresponding crack growth cycle. $\Delta K_\sigma^{\max}$ was calculated from the results of K_I and K_{II}, shown in Fig. 8, using Eqs. (11) and (13). The data given in Table 2 confirm that crack growth leads to an increase in $\Delta K_\sigma^{\max}$ and crack propagation direction at $q \approx 57$ deg.

To examine the dependence of the crack growth direction (i.e., direction of $\Delta K_\sigma^{\max}$) on the magnitude of crack growth increment, crack paths obtained for $\Delta c = h_1/4$, $h_1/8$, and $h_1/16$, $c_i/h_1 = 0.25$, and $m = m_c = 0.5$ are compared in Fig. 9. It is interesting to note that, after the first or second crack increments, the crack growth paths become almost parallel to each other, showing a common deviation angle from the direction normal to the free surface of ~57 deg. This suggests

that the crack growth increment does not affect the crack propagation direction. The obtained crack growth path is consistent with experimental observations of Ko et al. [17] according to which, crack growth commences at an angle of ~30 deg. with respect to the sliding direction, i.e., 60 deg. from the direction normal to the surface versus 57 deg. predicted in the present study. Moreover, the simulated crack propagation toward the interface is in qualitative agreement with numerical results reported by Oliveira and Bower [12] for fracture of thin coatings due to contact loading.

3.5 Fatigue Life Model

The finite element results presented above can be used in conjunction with the Euler integration algorithm discussed in section 2.4 to derive a contact fatigue model. While in the finite element simulations the crack grows by an increment Δc in each asperity passage, in reality crack growth commences after several asperity passes. To model this phenomenon using the simulation results, it is assumed that $\Delta K^{\max}$ (either tensile or shear, depending on which is larger) remains constant during crack propagation by Δc, and the actual number of asperity passes, i.e., fatigue cycles, is calculated from Eq. (9). To demonstrate this approach, a graphite substrate coated with a pyrolytic carbon layer was selected for analysis because it consists of an elastic (hard/brittle) carbon layer and an elastic-plastic (soft/ductile) graphite substrate. The fatigue properties of pyrolytic carbon, $m = 19$ and $A = 1.86 \times 10^{-18}$ m/cycle $(\text{MPa}\sqrt{\text{m}})^{-19}$, quoted from the study of Ritchie and Dauskardt [26], were used in the calculations. The normalized number of fatigue crack growth cycles, N^*, is given by

$$N^* \equiv \frac{A}{h_1}\left(\frac{2P}{\pi a^{1/2}}\right)^m N = \sum_{j=1}^{n} \frac{\Delta c / h_1}{D_j^m}, \qquad (15)$$

where N is obtained from Eqs. (9) and (10), and $D_j = \Delta K_s^{\max}(c_j)/(2P/pa^{1/2})$ is the normalized SIF range. Figure 10 shows the variation of normalized crack length, c/h_1, with N^* for $c_i/h_1 = 0.25$ and $\Delta c = h_1/8$. The very steep slope of the fatigue curve observed after the first few crack increments is indicative of the brittle behavior of pyrolytic carbon.

3.6 Evolution of Crack-Tip Stresses

Results for the stress field at the crack tip, obtained at different stages of the simulated crack growth process, are presented next for $c_i/h_1 = 0.25$, $\Delta c = h_1/8$, and $m = m_c = 0.5$. Figure 11 shows contours of von Mises equivalent stress in the vicinity of the crack tip produced in the first crack growth cycle. When the crack is adjacent to the trailing edge of the contact region ($y_P/a = 1.26$), it remains fully open (Fig. 11(a)) and the intensified stresses at the crack tip produce the maximum value of K_I shown in Fig. 3(a). However, when the asperity slides further to the right ($y_P/a = 5.88$), the crack faces move closer to each other (stress relaxation) and the size of the high-stress region at the crack tip decreases (Fig. 11(b)). This crack behavior is attributed to the high tensile stress at the trailing edge of the contact region (sliding friction effect), which decreases rapidly with the increase of the distance from the contact edge. Since the high stresses at the crack tip occur remote from the interface during the initial stage of crack growth, the crack-tip stresses do not affect the accumulation of plastic deformation in the second layer during sliding contact.

Figure 12 shows contours of von Mises equivalent stress in the eighth crack growth cycle, revealing remarkable changes in the stress field at the crack tip due to the propagation of the crack close to the interface. Conversely to the initial stage of crack growth, Fig. 12(a) shows that the crack remains partially open when it is close to the trailing edge of the contact region

($y_P / a = 1.26$), while Fig. 12(b) shows that the crack opens fully when the asperity moves further to the right ($y_P / a = 2.52$). This behavior is consistent with the fact that the maximum value of K_I in this case occurs at $y_P / a = 2.52$ (Fig. 8(a)) and is a consequence of the change of the crack propagation direction. In addition, the high-stress region at the crack tip is very close to the interface, affecting the stresses in the second layer. The large stress discontinuities at the interface (Fig. 12(b)) are due to the significant elastic modulus mismatch of the two layers. The intensification of the stress field in the second layer as the crack propagates closer to the interface affects the deformation in the second layer adjacent to the interface. This phenomenon is discussed in detail in the following section.

3.7 Development of Plasticity in the Second Layer

The effects of crack length, friction at the contact region and crack interface, and sliding cycles on the deformation of the elastic-plastic second layer are examined in this section. It is noted that for the loading conditions and layer material properties used in this study, the deformation in the third and fourth elastic-plastic layers is purely elastic. Thus, stress/strain results for these layers are not presented here for the sake of brevity.

Figure 13(a) shows the maximum equivalent plastic strain, $\bar{e}_p^{\max}$, in the second layer versus dimensionless asperity position and crack length for $m = m_c = 0.5$. In all cases, $\bar{e}_p^{\max}$ increases as the asperity slides over the multi-layered medium in a similar fashion, reaching a steady state at a distance from the crack approximately equal to five times the half-contact width. The results show that the accumulation of plasticity does not depend on the (initial) crack length, evidently because the high-stress field at the crack tip is far away from the interface (when the crack is relatively short) to affect deformation in the second layer. Thus, the crack effect on the

propensity for plastic flow in the second layer is negligible until the crack tip reaches a distance less than $h_1/8$ from the interface, as shown by the simulation results. The location of $\bar{e}_p^{\max}$ in the second layer is always at the interface with the first layer below the asperity and shifts along the interface as the asperity slides over the medium, in agreement with a previous finite element analysis of normal and sliding contact of a rigid cylindrical asperity on a patterned elastic-plastic layered medium [5].

Figure 13(b) shows the variation of $\bar{e}_p^{\max}$ in the second layer with dimensionless asperity position and coefficient of friction at the contact region and crack interface for $c_i / h_1 = 0.125$. As the asperity slides on the surface of the multi-layered medium, $\bar{e}_p^{\max}$ increases monotonically, exhibiting a trend similar to that shown in Fig. 13(a). As expected, $\bar{e}_p^{\max}$ intensifies with the increase of coefficient of friction at the contact region due to the pronounced effect of the surface shear (friction) traction on the subsurface stress field. However, the effect of crack-face friction is negligible because it only affects the stress field at the crack tip, which, in this case, is far away from the interface to affect the stress state in the second layer. Therefore, only friction at the contact region affects the accumulation of plasticity in the second layer when the crack tip is remote from the layer interface.

Figure 14 shows contours of $\bar{e}_p$ in the second layer obtained in the eighth crack growth cycle for two asperity positions, $c_i / h_1 = 0.25$, $\Delta c = h_1 / 8$, and $m = m_c = 0.5$. When the crack is just behind the trailing edge of the contact region ($y_P / a = 1.26$), the crack is partially closed and $\bar{e}_p^{\max}$ arises below the crack tip, adjacent to the interface with the first layer (Fig. 14(a)). However, when the asperity moves further away from the crack ($y_P / a = 2.52$), the crack opens

fully, while $\bar{e}_p^{\max}$ occurs again below the crack tip close to the interface (Fig. 14(b)). This differs from the results of previous crack growth cycles showing that $\bar{e}_p^{\max}$ shifts along the interface under the moving asperity. This finding provides additional evidence for the effect of crack-tip stresses on the evolution of plasticity in the second layer.

In the case of multiple asperity contacts, knowledge of the accumulation of plasticity in the multi-layered medium is of particular importance. The results of the present analysis can be used to examine the evolution of plasticity in the second layer due to multi-asperity contacts with spacing larger than the average contact width. Figure 15(a) shows $\bar{e}_p^{\max}$ in the second layer versus dimensionless asperity position for different crack growth cycles, $c_i / h_1 = 0.25$, $\Delta c = h_1 / 8$, and $m = m_c = 0.5$. A gradual increase in $\bar{e}_p^{\max}$ occurs when the asperity slides over the medium and with the increase of crack growth cycles (i.e., crack propagation). The increments of $\bar{e}_p^{\max}$ decrease with increasing crack growth cycles because the crack tip is remote from the interface to affect the development of plasticity. However, in the eighth crack growth cycle, a sharp increase in $\bar{e}_p^{\max}$ is encountered when the asperity slides over the crack due to the small distance of the high-stress region at the crack tip from the interface. To better illustrate the effect of crack-tip stresses on the evolution of plastic deformation in the second layer, the increment of maximum plastic strain, $\Delta\bar{e}_p^{\max}$, is plotted as a function of number of (simulated) crack growth cycles, *n*, in Fig. 15(b). The decrease of $\Delta\bar{e}_p^{\max}$ up to the seventh crack growth cycle reveals the dominant effect of repetitive sliding, while the sharp increase of $\Delta\bar{e}_p^{\max}$ in the eight crack growth cycle, i.e., when the crack propagates very close to the interface, illustrates the effect of the

crack-tip stresses on plastic flow in the second layer, within a small region close to the interface with the first layer.

While the present analysis provides insight into surface cracking in elastic-plastic multi-layered media subjected to cyclic loading, the obtained results can be used to discuss possible failure mechanisms. For instance, when the crack propagates to the interface, failure may occur due to delamination along the weaker interface, resulting in the formation of a sheet-like wear particle. Assuming that the fatigue life is dominated by crack growth in the first layer, i.e., layer debonding occurs rapidly after the crack reaches the interface, the fracture approach presented in this study can be used to estimate the loading cycles required to form a wear particle. However, in the case of high interfacial strength, the crack may propagate into the second layer, where it may become inactive or shear eventually toward the surface to produce a wear particle, as in the case of homogeneous media [17], depending on the stress field. Crack growth in the elastic-plastic second layer can be accomplished with appropriate modification of the finite element mesh used in this analysis.

4. Conclusions

Surface cracking in a multi-layered medium containing a crack perpendicular to the free surface due to repetitive sliding of a rigid asperity was analyzed using linear elastic fracture mechanics and the finite element method. Based on the presented results and discussion, the following main conclusions can be drawn from this study.

1. The significantly higher values (by an order of magnitude) of the tensile stress intensity factor, K_I, than those of the shear stress intensity factor, K_{II}, obtained in all simulation cases indicate that surface cracking in the multi-layered medium due to sliding contact is controlled by the tensile fracture mode.

2. Longer surface cracks produce significantly higher K_I values and marginally different K_{II} values. Higher friction at the sliding contact region increases both K_I and K_{II} significantly due to the strong effect of the surface shear traction on the crack-tip stresses. The increase of friction at the crack interface promotes stress relaxation that decreases the magnitude of K_{II}; however, the effect on K_I is negligible.
3. Based on the maximum tensile stress intensity range, $\Delta K_s^{\max}$, initial crack growth was found to occur at an angle of ~10 deg. from the original crack plane, independent of initial crack length. Although the crack length effect on the crack growth direction is negligible, the effect on the magnitudes of $\Delta K_\sigma^{\max}$ and $\Delta K_\tau^{\max}$ is significant.
4. After the first few (1-3) crack growth increments, the crack growth paths obtained with different propagation increments become almost parallel to each other, exhibiting a common deviation angle from the original crack plane of ~57 deg., in fair agreement with experimental observations.
5. Crack growth increases the magnitudes of K_I and ΔK_s. An approach for estimating the contact fatigue life due to surface crack growth in multi-layered media was derived from the finite element results, and its application was demonstrated by fatigue crack growth results obtained for a graphite substrate coated with a pyrolitic carbon layer.
6. The effect of initial crack length on plastic deformation in the elastic-plastic second layer is negligible because the crack-tip stresses do not reach the layer interface. The effect becomes significant only when the crack propagates very close to the interface, a distance approximately less than one-eighth of the first layer thickness. The coefficient of friction at

the contact (sliding) region exhibits a dominant effect on the plastic strain accumulating in the second layer, while the effect of crack-face friction is insignificant.

7. The maximum plastic strain in the second layer increases rapidly as the crack tip approaches the interface due to the effect of the high-stress field at the crack tip. This causes the maximum plastic strain in the second layer to arise always below the crack tip adjacent to the interface rather than below the sliding asperity, as found for uncracked elastic-plastic layered media in earlier studies.

Acknowledgments

This research was funded by the National Science Foundation under a subcontract through Carnegie Mellon University, Award No. 1002071-105936, and the Computer Mechanics Laboratory at the University of California at Berkeley.

References

[1] King, R. B., and O'Sullivan, T. C., 1987, "Sliding Contact Stresses in a Two-Dimensional Layered Elastic Half-Space," Int. J. Solids Struct., **23**, pp. 581-597.

[2] Kral, E. R., and Komvopoulos, K., 1996, "Three-Dimensional Finite Element Analysis of Surface Deformation and Stresses in an Elastic-Plastic Layered Medium Subjected to Indentation and Sliding Contact Loading," ASME J. Appl. Mech., **63**, pp. 365-375.

[3] Lawn, B., 1992, "Friction Processes in Brittle Fracture," Fundamentals of Friction: Macroscopic and Microscopic Processes, Singer, I. L., and Pollock, H. M., Eds., NATO ASI Series E: Appl. Sci., **220**, pp. 137-165.

[4] Wu, T. W., 1991, "Microscratch and Load Relaxation Tests for Ultra-thin Films," J. Mater. Res., **6**, pp. 407-426.

[5] Gong, Z.-Q., and Komvopoulos, K., 2003, "Effect of Surface Patterning on Contact Deformation of Elastic-Plastic Layered Media," ASME J. Tribol., **125**, pp. 16-24.

[6] Gong, Z.-Q., and Komvopoulos, K., 2004, "Mechanical and Thermomechanical Elastic-Plastic Contact Analysis of Layered Media with Patterned Surfaces," ASME J. Tribol., **126**, in press.

[7] Keer, L. M., and Worden, R. E., 1990, " A Qualitative Model to Describe the Microchipping Wear Mode in Ceramic Rollers," Tribol. Trans., **33**, pp. 411-417.

[8] Keer, L. M., and Kuo, C. H., 1992, "Cracking in a Loaded Brittle Elastic Half-Space," Int. J. Solids Struct., **29**, pp. 1819-1826.

[9] Chen, S. Y., Farris, T. N., and Chandrasekar, S., 1991, "Sliding Microindentation Fracture of Brittle Materials," Tribol. Trans., **34**, pp. 161-168.

[10] Bower, A. F., and Fleck, N. A., 1994, "Brittle Fracture Under a Sliding Line Contact," J. Mech. Phys. Solids, **42**, pp. 1375-1396.

[11] Beuth, J. L., and Klingbeil, N. W., 1996, "Cracking of Thin Films Bonded to Elastic-Plastic Substrates," J. Mech. Phys. Solids, **44**, pp. 1411-1428.

[12] Oliveira, S. A. G., and Bower, A. F., 1996, "An Analysis of Fracture and Delamination in Thin Coatings Subjected to Contact Loading," Wear, **198**, pp. 15-32.

[13] Mageed, A. M. A., and Pandey, R. K., 1992, "Studies on Cyclic Crack Path and the Mixed-Mode Crack Closure Behavior in Al Alloy," Int. J. Fatig., **14**, pp. 21-29.

[14] Alfredsson, B., and Olsson, M., 2000, "Initiation and Growth of Standing Contact Fatigue Cracks," Eng. Fract. Mech., **65**, pp. 89-106.

[15] Lin, X. B., and Smith, R. A., 1999, "Finite Element Modelling of Fatigue Crack Growth of Surface Cracked Plates, Part I: The Numerical Technique," Eng. Fract. Mech., **63**, pp. 503-522.

[16] Lin, X. B., and Smith, R. A., 1999, "Finite Element Modelling of Fatigue Crack Growth of Surface Cracked Plates, Part III: Stress Intensity Factor and Fatigue Crack Growth Life," Eng. Fract. Mech., **63**, pp. 541-556.

[17] Ko, P. L., Iyer, S. S., Vaughan, H., and Gadala, M., 2001, "Finite Element Modelling of Crack Growth and Wear Particle Formation in Sliding Contact," Wear, **251**, pp. 1265-1278.

[18] Komvopoulos, K., and Choi, D.–H., 1992, "Elastic Finite Element Analysis of Multi-Asperity Contacts," ASME J. Tribol., **114**, pp. 823-831.

[19] Henshell, R. D., and Shaw, K. G., 1975, "Crack Tip Finite Elements Are Unnecessary," Int. J. Numer. Meth. Eng., **9**, pp. 495-507.

[20] Barsoum, R. S., 1976, "On the Use of Isoparametric Finite Elements in Linear Fracture Mechanics," Int. J. Numer. Meth. Eng., **10**, pp. 25-37.

[21] Hertzberg, R. W., 1996, *Deformation and Fracture Mechanics of Engineering Materials*, Wiley, New York.

[22] Chan, S. K., Tuba, I. S., and Wilson, W. K., 1970, "On the Finite Element Method in Linear Fracture Mechanics," Eng. Fract. Mech., **2**, pp. 1-17.

[23] Komvopoulos, K., and Cho, S. -S., 1997, "Finite Element Analysis of Subsurface Crack Propagation in a Half-Space due to a Moving Asperity Contact," Wear, **209**, pp. 57-68.

[24] Paris, P., and Erdogan, F., 1963, "A Critical Analysis of Crack Propagation Laws," ASME J. Basic Eng., **85**, pp. 528-534.

[25] Erdogan, F., and Sih, G. C., 1963, "On the Crack Extension in Plates Under Plane Loading and Transverse Shear," J. Basic Eng., **85**, pp. 519-527.

[26] Ritchie, R. O., and Dauskardt, R. H., 1991, "Cyclic Fatigue of Ceramics: a Fracture Mechanics Approach to Subcritical Crack Growth and Life Prediction," J. Ceram. Soc. Japan, **99**, pp. 1047-1062.

Table 1. Thickness and material properties of each layer in the multi-layered medium

Layer	h/R	E (GPa)	s_Y (GPa)
1	0.025	260	-
2	0.078	130	2.67
3	0.4	140	2.58
4	2.6	160	2.67

Table 2. Current crack deviation angle, total deviation angle, and maximum tensile stress intensity factor range versus crack growth cycle for $c_i / h_1 = 0.25$, $\Delta c = h_1 / 8$, and $m = m_c = 0.5$

Crack growth cycle	Δq (deg.)	q_{total}(deg.)	$\Delta K_\sigma^{\max} / (2P/\pi a^{1/2})$
1	11	11	0.5342
2	28	39	0.7462
3	18	57	0.9947
4	-8	49	1.0256
5	8	57	1.1281
6	-8	49	1.1416
7	8	57	1.2397
8	-6	51	1.2778

List of Figures

Fig. 8 Dimensionless tensile and shear stress intensity factors, K_I and K_{II}, respectively, versus crack growth cycle and dimensionless asperity position, y_P / a, for $c_i / h_1 = 0.25$, $\Delta c = h_1 / 8$, and $m = m_c = 0.5$.

Fig. 9 Simulated crack paths for crack growth increment Δc = h_1/4, h_1/8, and h_1/16, $c_i / h_1 = 0.25$, and $m = m_c = 0.5$.

Fig. 10 Dimensionless crack length, c / h_1, versus dimensionless number of estimated fatigue crack growth cycles, N*, for pyrolytic carbon-coated graphite, $c_i / h_1 = 0.25$, $\Delta c = h_1 / 8$, and $m = m_c = 0.5$.

Fig. 11 Contours of von Mises equivalent stress, s_M, in the vicinity of the crack tip obtained in the first crack growth cycle for $c_i / h_1 = 0.25$, $\Delta c = h_1 / 8$, $m = m_c = 0.5$, and dimensionless asperity position (a) $y_P / a = 1.26$ and (b) $y_P / a = 5.88$.

Fig. 12 Contours of von Mises equivalent stress, s_M, in the vicinity of the crack tip obtained in the eighth crack growth cycle for $c_i / h_1 = 0.25$, $\Delta c = h_1 / 8$, $m = m_c = 0.5$, and dimensionless asperity position (a) $y_P / a = 1.26$ and (b) $y_P / a = 2.52$.

Fig. 13 Maximum equivalent plastic strain, $\bar{e}_p^{\max}$, in the elastic-plastic second layer versus dimensionless asperity position, y_P / a: (a) c_i/h_1 = 0.125, 0.25, 0.5, and 0.875 and $m = m_c = 0.5$, and (b) c_i/h_1 = 0.125, m = 0.1, 0.25, and 0.5, and m_c = 0 and 0.5.

Fig. 14 Contours of equivalent plastic strain, $\bar{e}_p$, in the elastic-plastic second layer obtained in the eighth crack growth cycle for $c_i / h_1 = 0.25$, $\Delta c = h_1 / 8$, $m = m_c = 0.5$, and dimensionless asperity position (a) $y_P / a = 1.26$ and (b) $y_P / a = 2.52$.

Fig. 15 (a) Maximum equivalent plastic strain, $\bar{e}_p^{\max}$, in the elastic-plastic second layer versus dimensionless asperity position, y_P / a, for different simulated crack growth cycles, and (b) increment of maximum equivalent plastic strain, $\Delta\bar{e}_p^{\max}$, in the elastic-plastic second layer versus number of simulated crack growth cycles, n. (The results shown in (a) and (b) are for $c_i / h_1 = 0.25$, $\Delta c = h_1 / 8$, and $m = m_c = 0.5$).

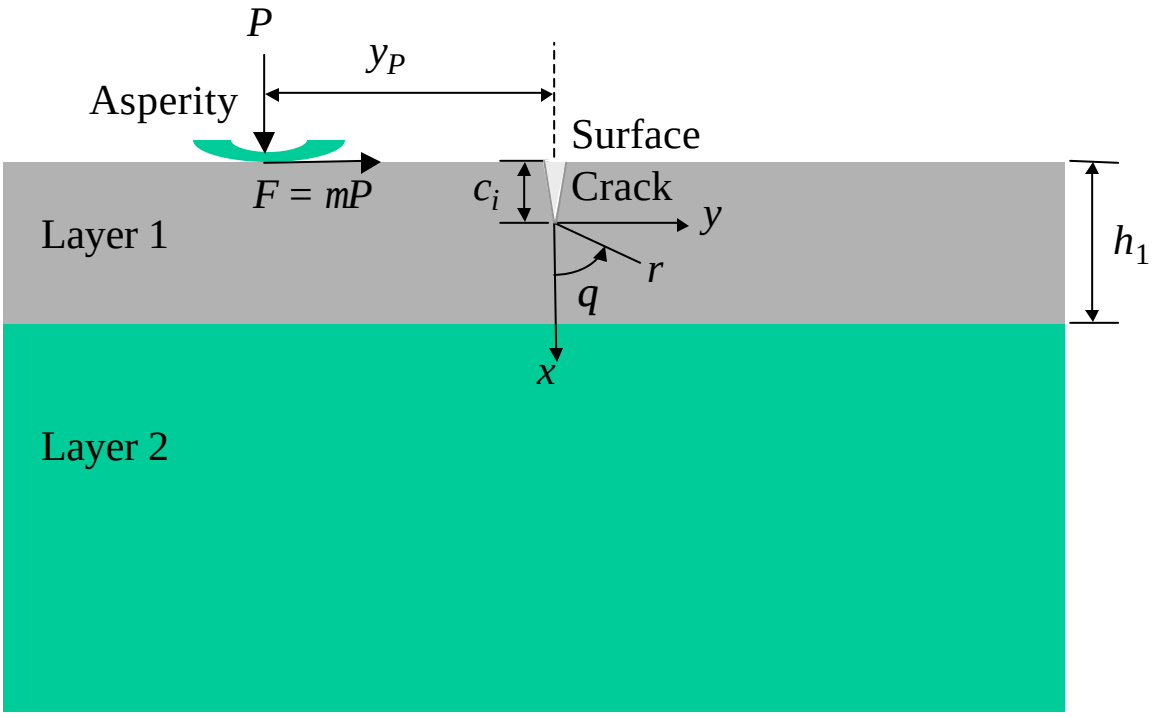

Figure 1

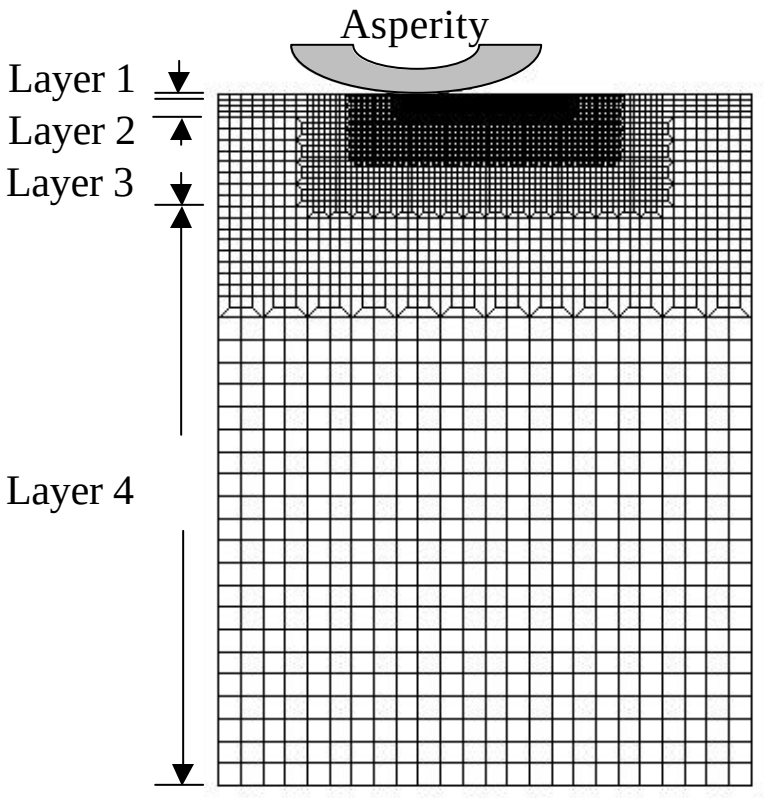

(*a*)

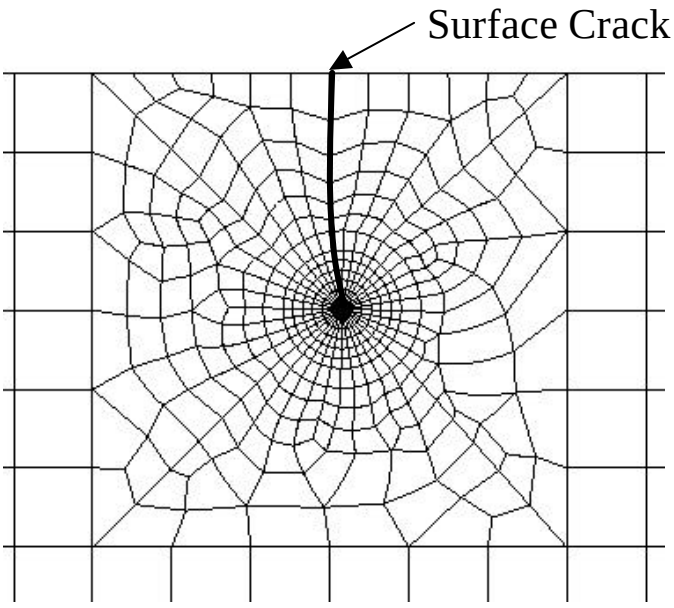

(*b*)

Figure 2

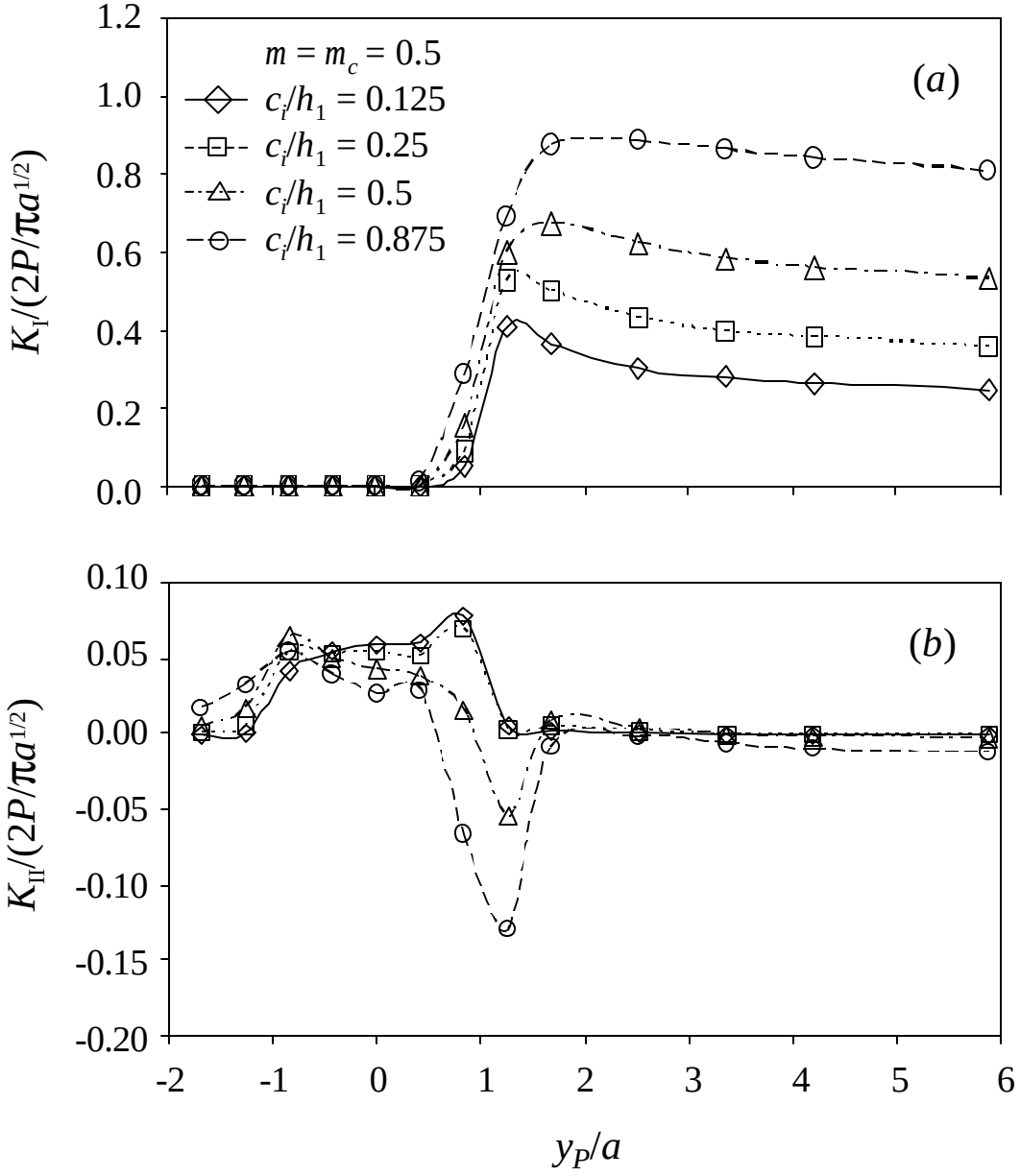
m = m_c = 0.5
c_i/h_1 = 0.125
c_i/h_1 = 0.25
c_i/h_1 = 0.5
c_i/h_1 = 0.875
(a)
(b)
K_I/(2P/πa^1/2)
K_II/(2P/πa^1/2)
y_P/a
1.2
1.0
0.8
0.6
0.4
0.2
0.0
0.10
0.05
0.00
-0.05
-0.10
-0.15
-0.20
-2
-1
0
1
2
3
4
5
6

Figure 3

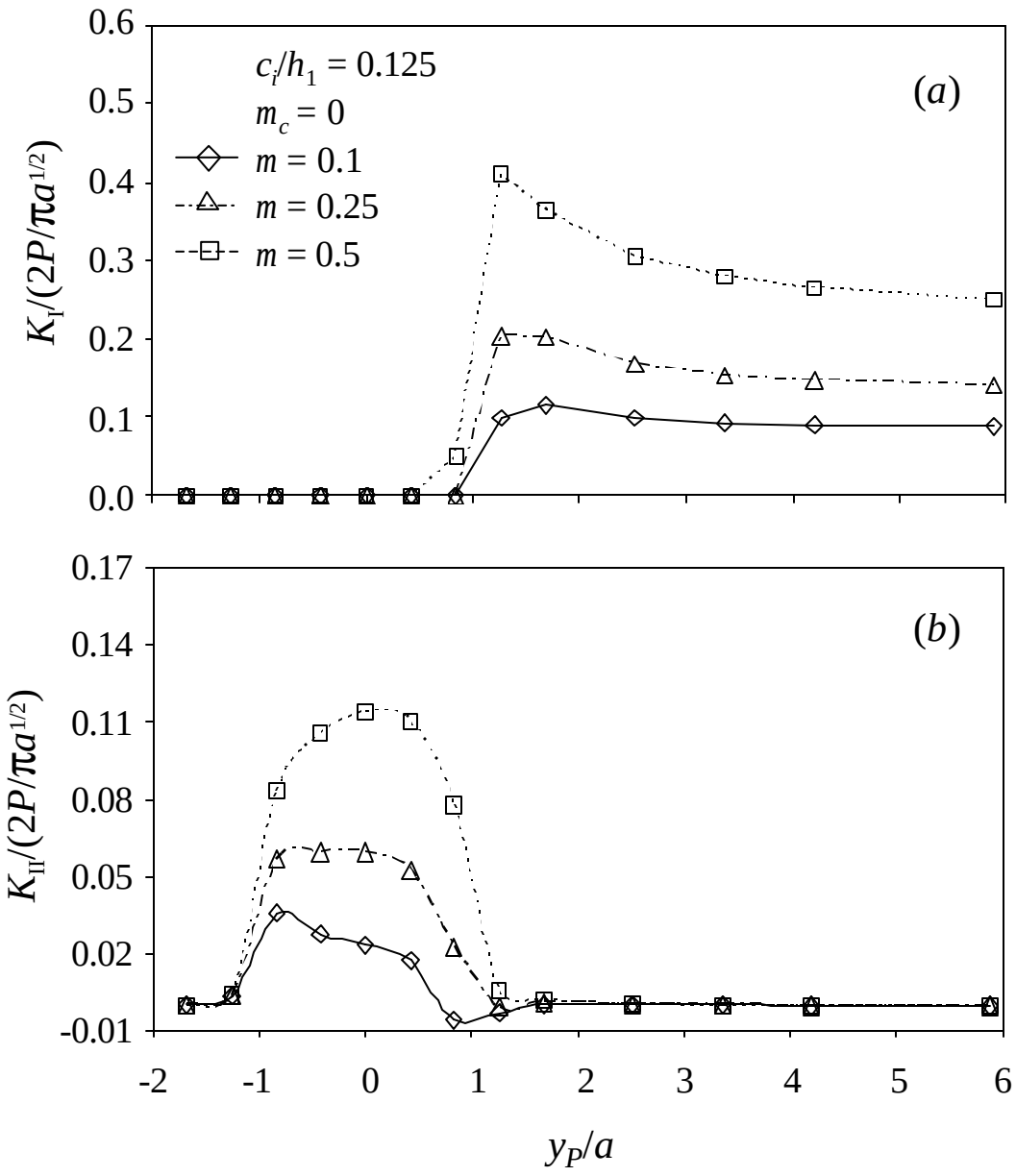
c_i/h_1 = 0.125
m_c = 0
m = 0.1
m = 0.25
m = 0.5
(a)
(b)
$K_I/(2P/\pi a^{1/2})$
$K_{II}/(2P/\pi a^{1/2})$
y_P/a
0.6
0.5
0.4
0.3
0.2
0.1
0.0
0.17
0.14
0.11
0.08
0.05
0.02
-0.01
-2
-1
0
1
2
3
4
5
6

Figure 4

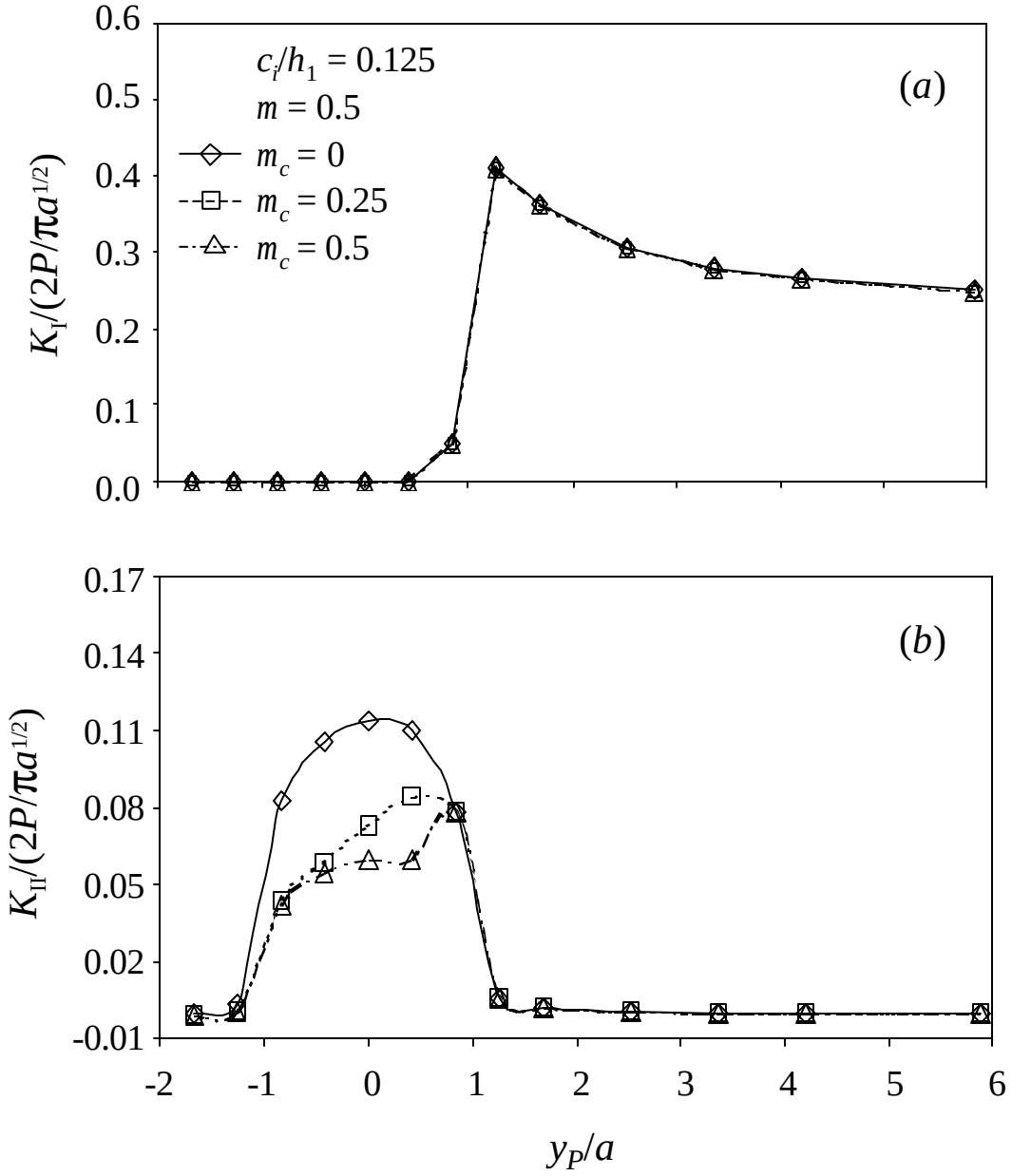
0.6
0.5
0.4
0.3
0.2
0.1
0.0
$c_i/h_1 = 0.125$
$m = 0.5$
$m_c = 0$
$m_c = 0.25$
$m_c = 0.5$
(a)
$K_I/(2P/\pi a^{1/2})$
0.17
0.14
0.11
0.08
0.05
0.02
-0.01
(b)
$K_{II}/(2P/\pi a^{1/2})$
-2
-1
0
1
2
3
4
5
6
y_P/a

Figure 5

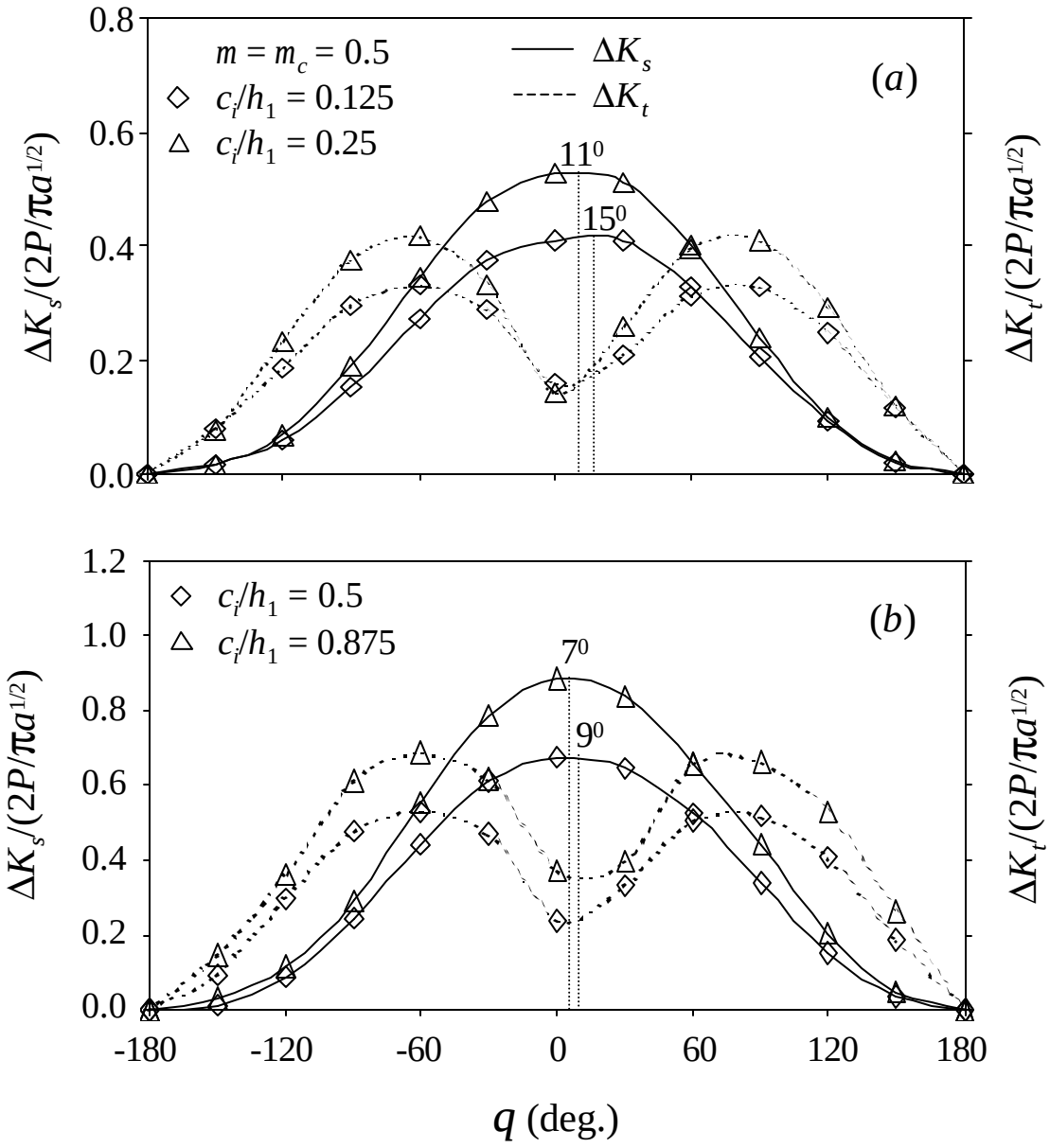
m = m_c = 0.5
c_i/h_1 = 0.125
c_i/h_1 = 0.25
ΔK_s
ΔK_t
(a)
11^0
15^0
ΔK_s/(2P/πa^1/2)
ΔK_t/(2P/πa^1/2)
0.0
0.2
0.4
0.6
0.8
c_i/h_1 = 0.5
c_i/h_1 = 0.875
(b)
7^0
9^0
1.0
1.2
-180
-120
-60
0
60
120
180
q (deg.)

Figure 6

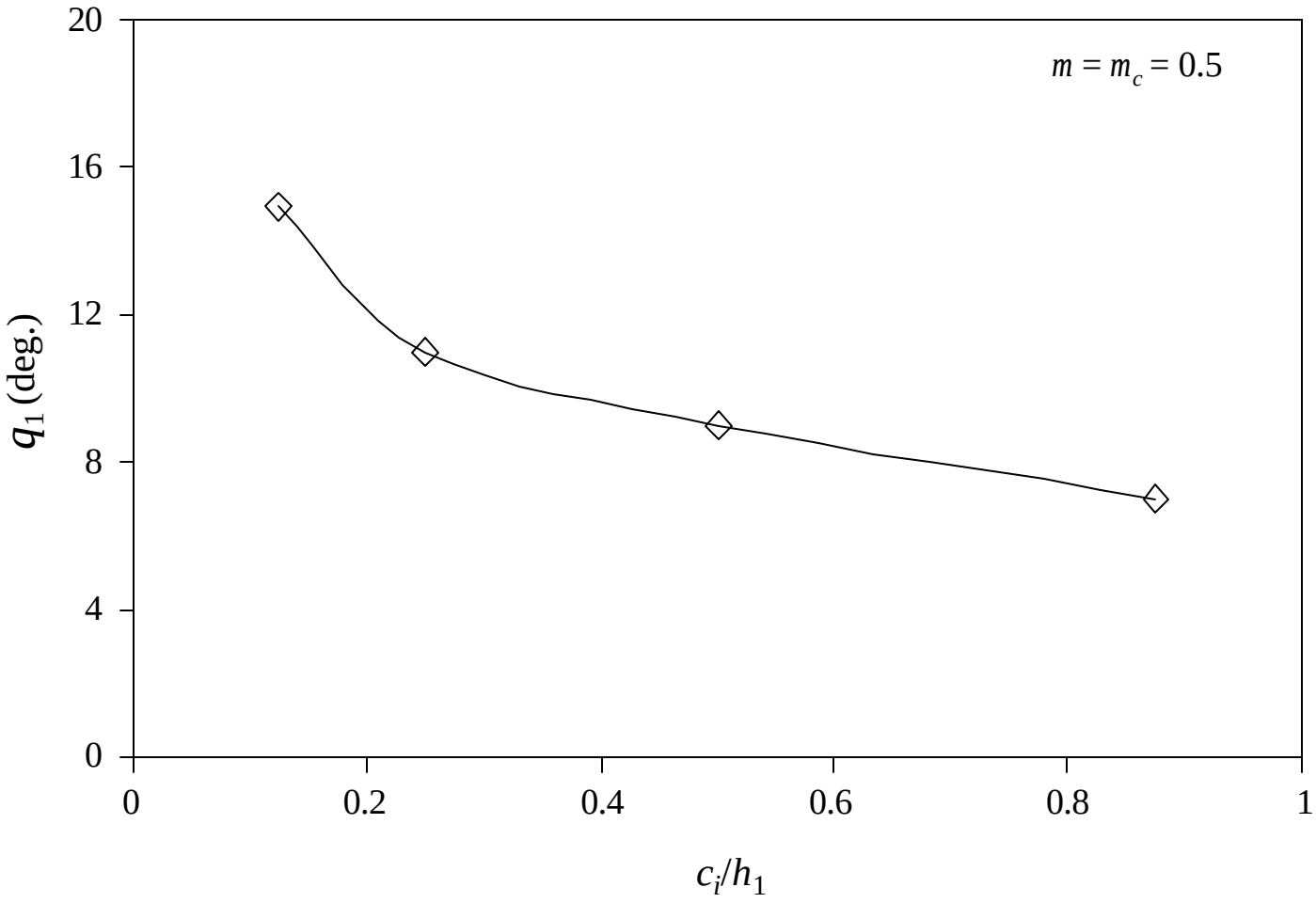

Figure 7

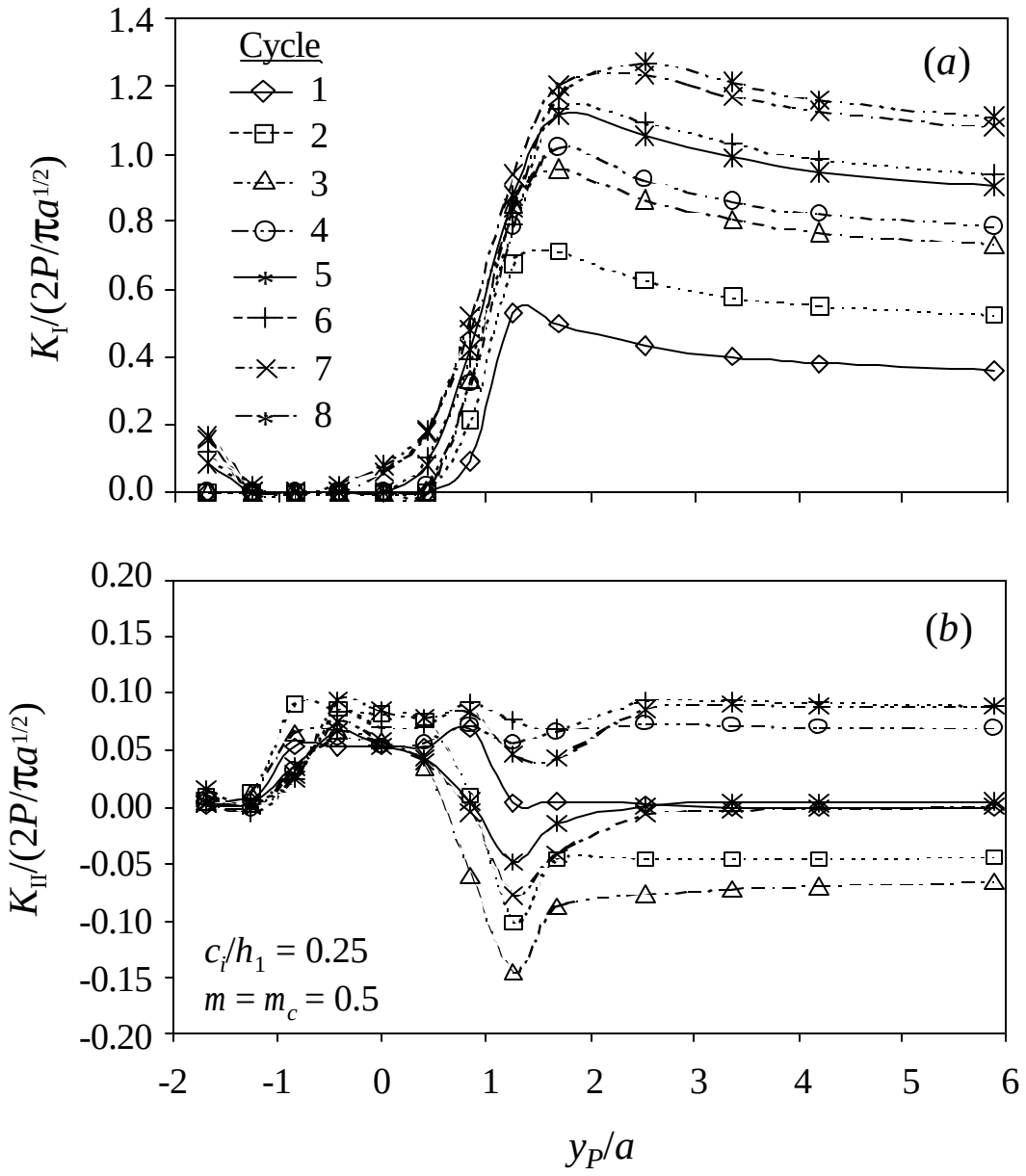
Cycle
1
2
3
4
5
6
7
8
(a)
$K_I/(2P/\pi a^{1/2})$
1.4
1.2
1.0
0.8
0.6
0.4
0.2
0.0
(b)
$K_{II}/(2P/\pi a^{1/2})$
0.20
0.15
0.10
0.05
0.00
-0.05
-0.10
-0.15
-0.20
$c_i/h_1 = 0.25$
$m = m_c = 0.5$
-2
-1
0
1
2
3
4
5
6
y_P/a

Figure 8

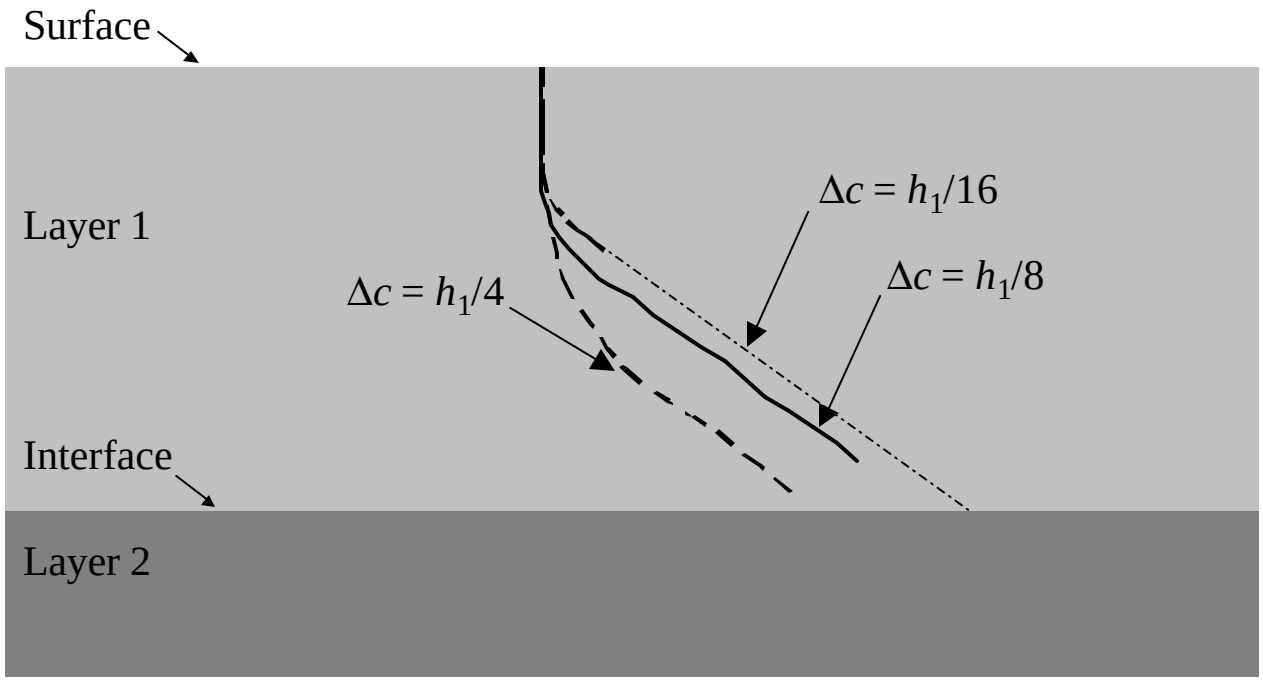

Figure 9

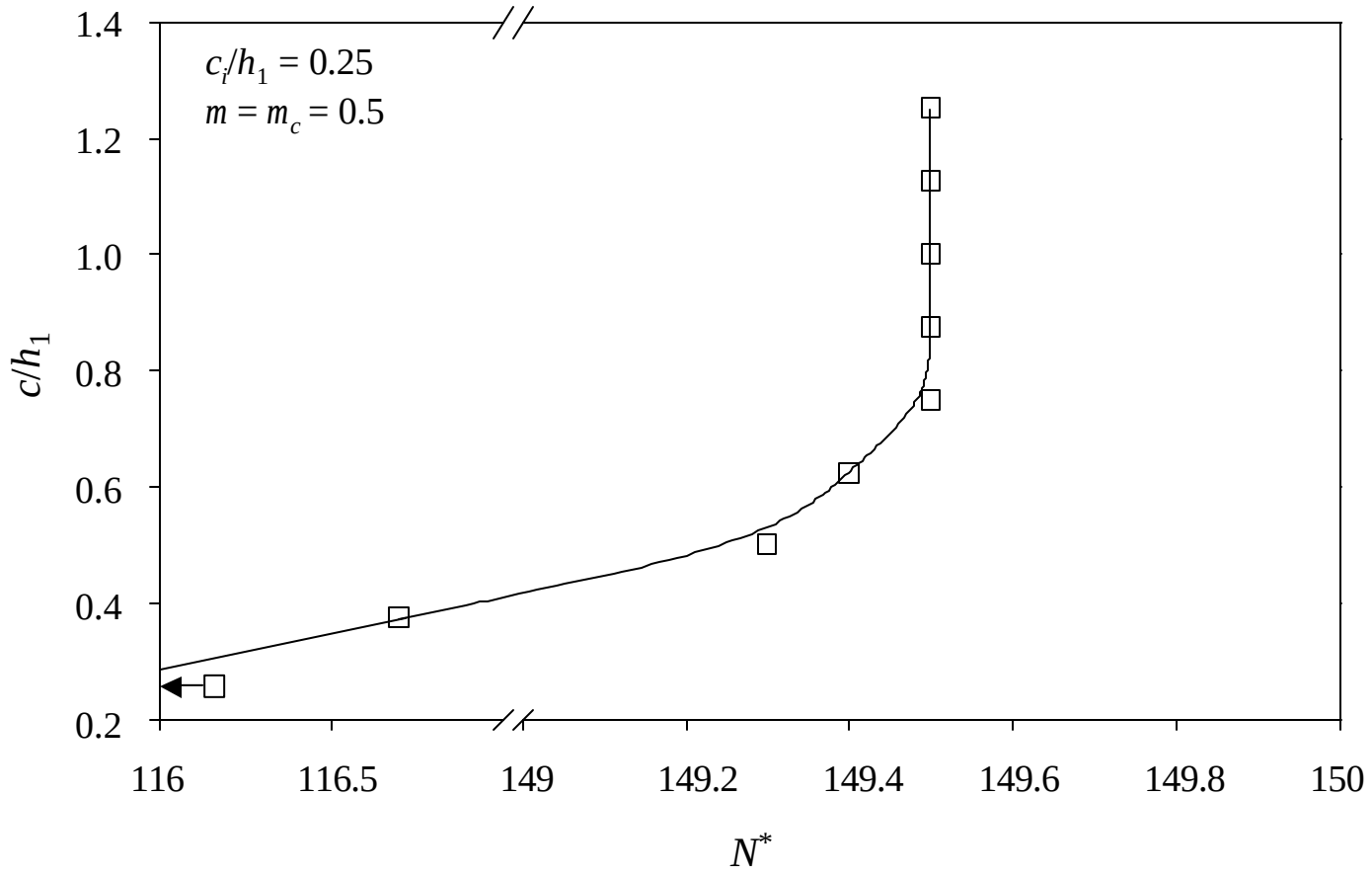
$c_i/h_1 = 0.25$
$m = m_c = 0.5$
c/h_1
1.4
1.2
1.0
0.8
0.6
0.4
0.2
116
116.5
149
149.2
149.4
149.6
149.8
150
N^*

Figure 10

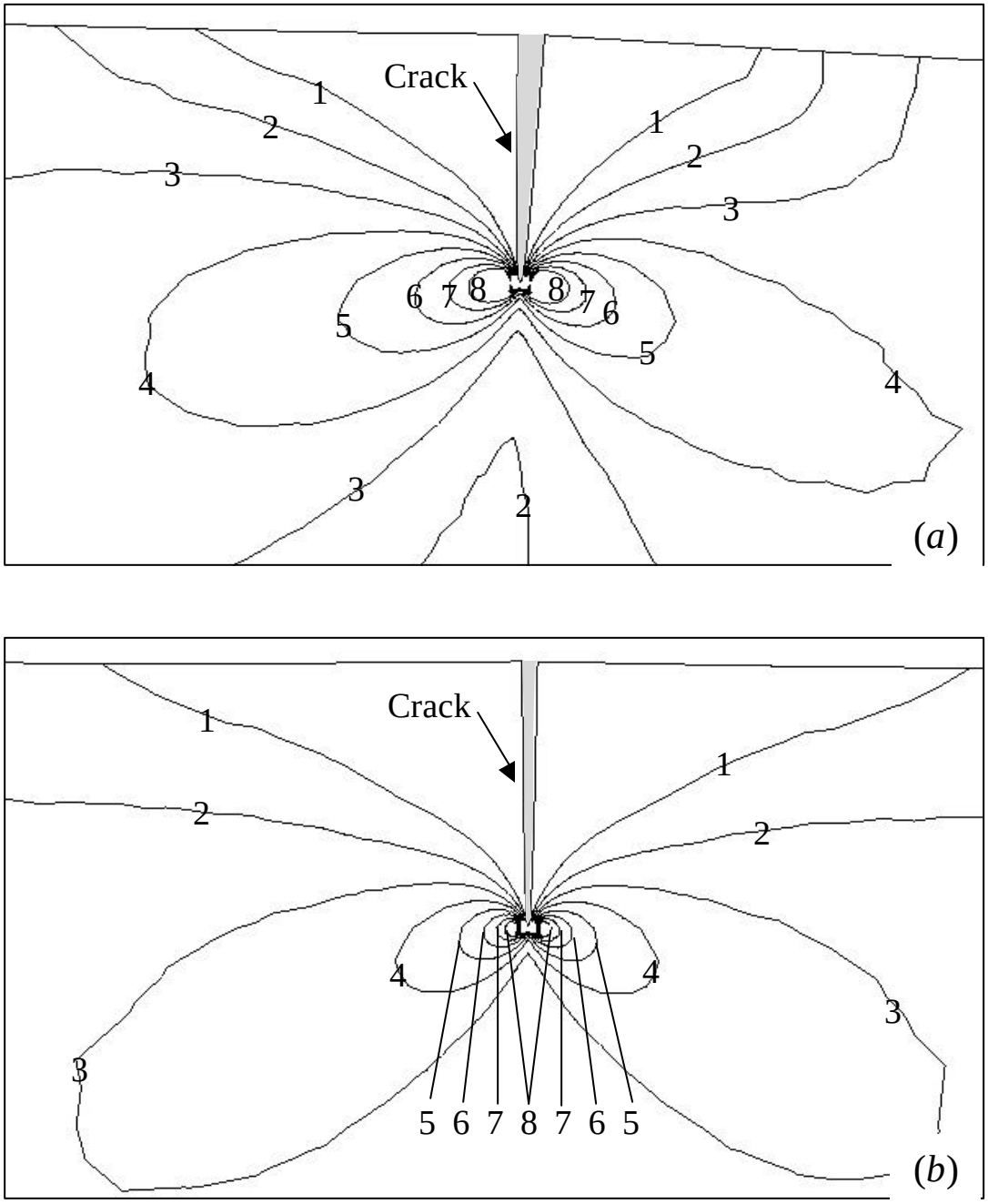

S_M (GPa)

(1) 1.0	(2) 2.0	(3) 3.0	(4) 4.0	(5) 5.0	(6) 6.0	(7) 7.0	(8) 8.0

Figure 11

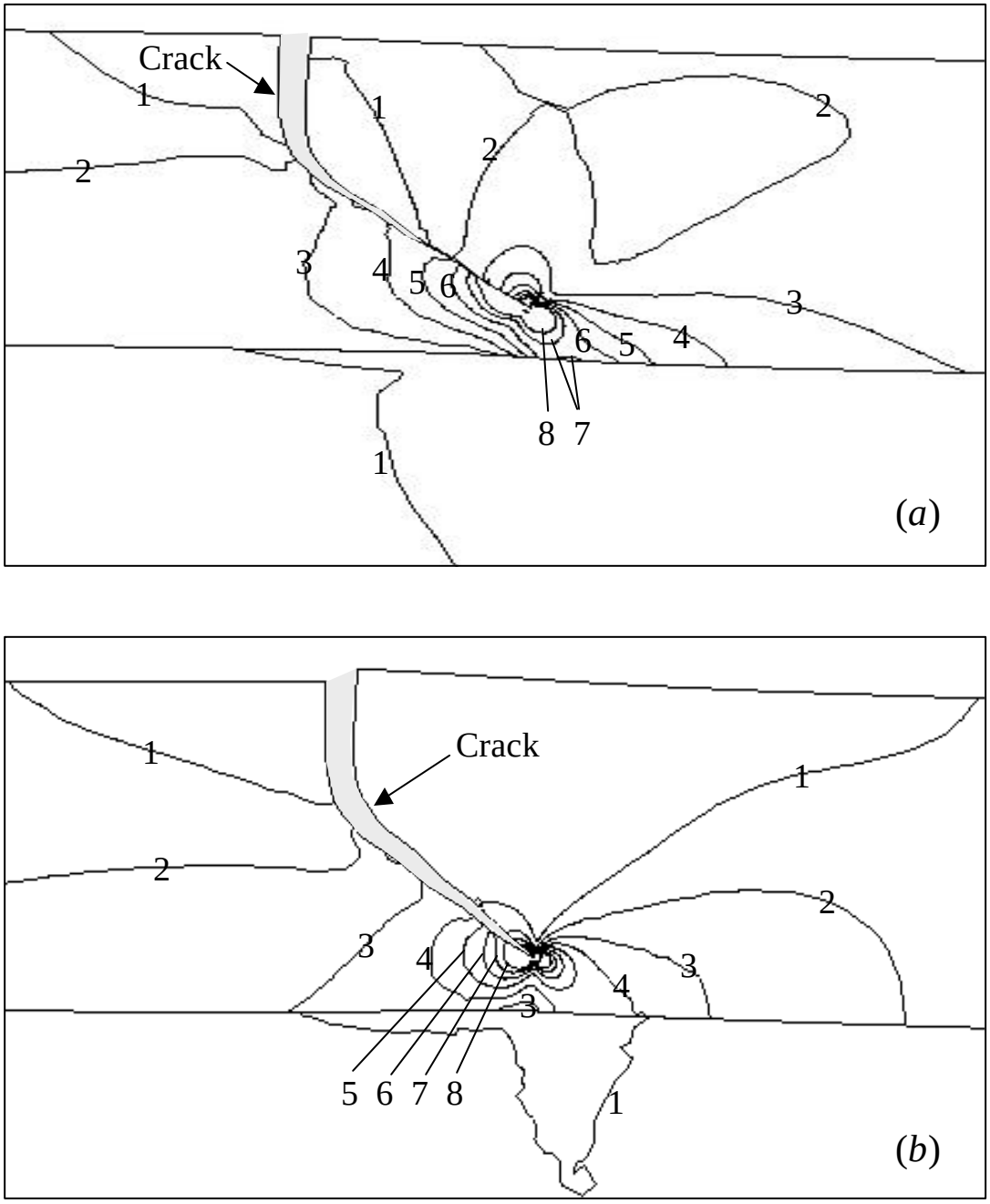

S_M (GPa)

(1) 1.88 (2) 3.75 (3) 5.63 (4) 7.50 (5) 9.38 (6) 11.3 (7) 13.1 (8) 15.0

Figure 12

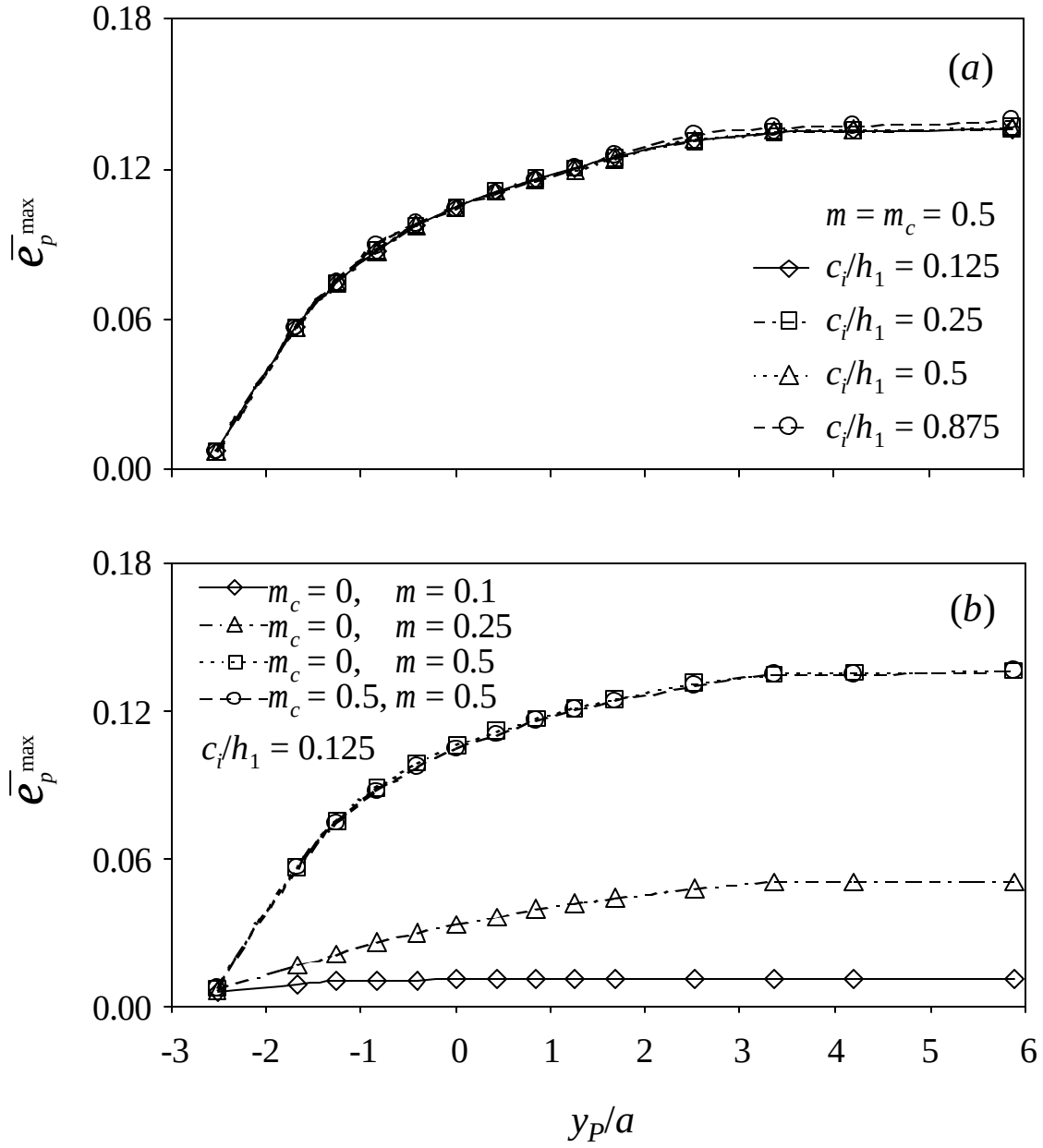
0.18
0.12
0.06
0.00
$\overline{e}_p^{\max}$
(a)
$m = m_c = 0.5$
$c_i/h_1 = 0.125$
$c_i/h_1 = 0.25$
$c_i/h_1 = 0.5$
$c_i/h_1 = 0.875$
0.18
0.12
0.06
0.00
$\overline{e}_p^{\max}$
(b)
$m_c = 0, \quad m = 0.1$
$m_c = 0, \quad m = 0.25$
$m_c = 0, \quad m = 0.5$
$m_c = 0.5, m = 0.5$
$c_i/h_1 = 0.125$
-3
-2
-1
0
1
2
3
4
5
6
y_P/a

Figure 13

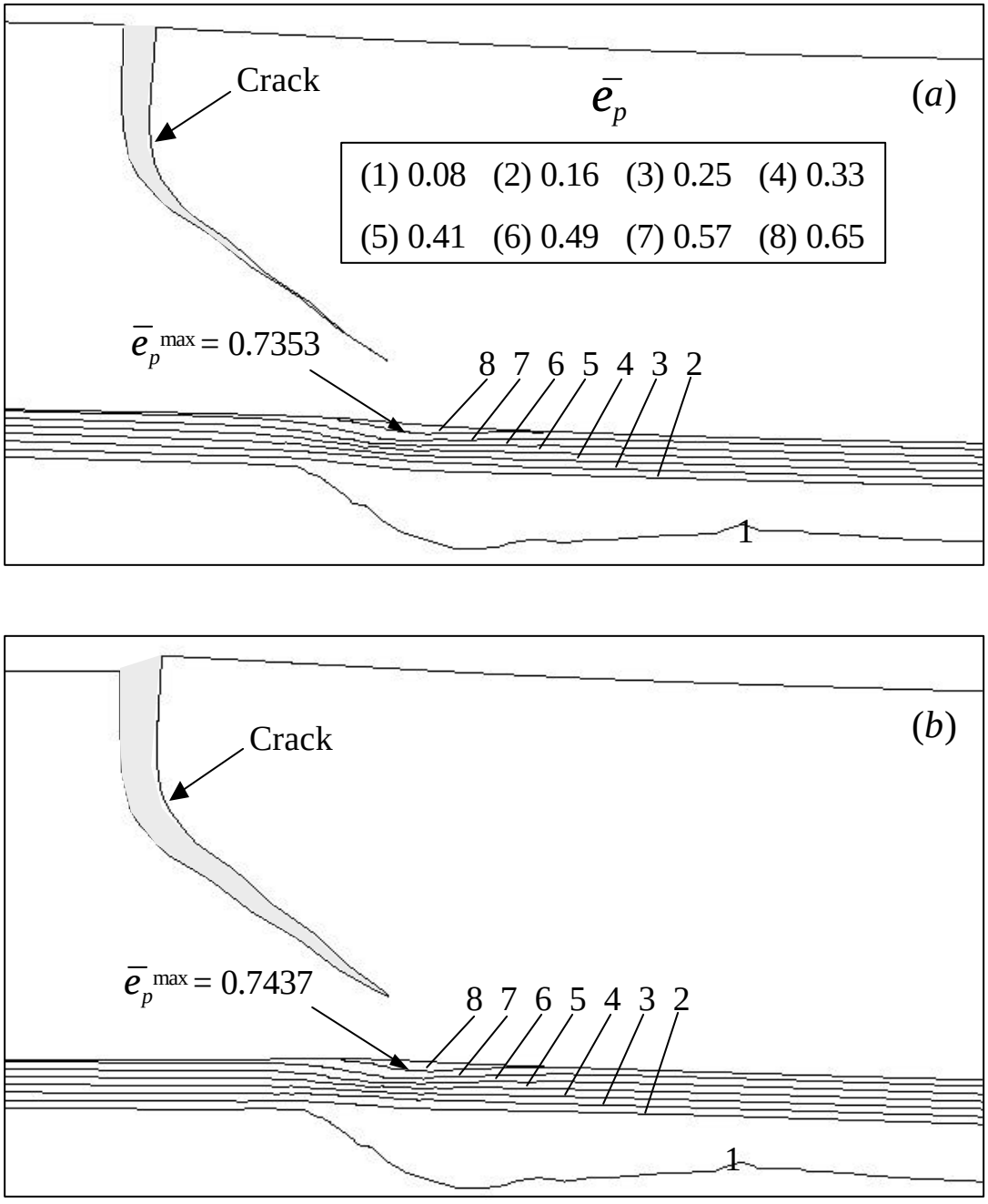
Crack
$\bar{e}_p$
(a)
(1) 0.08 (2) 0.16 (3) 0.25 (4) 0.33
(5) 0.41 (6) 0.49 (7) 0.57 (8) 0.65
$\bar{e}_p^{\max} = 0.7353$
8 7 6 5 4 3 2
1
Crack
(b)
$\bar{e}_p^{\max} = 0.7437$
8 7 6 5 4 3 2
1

Figure 14

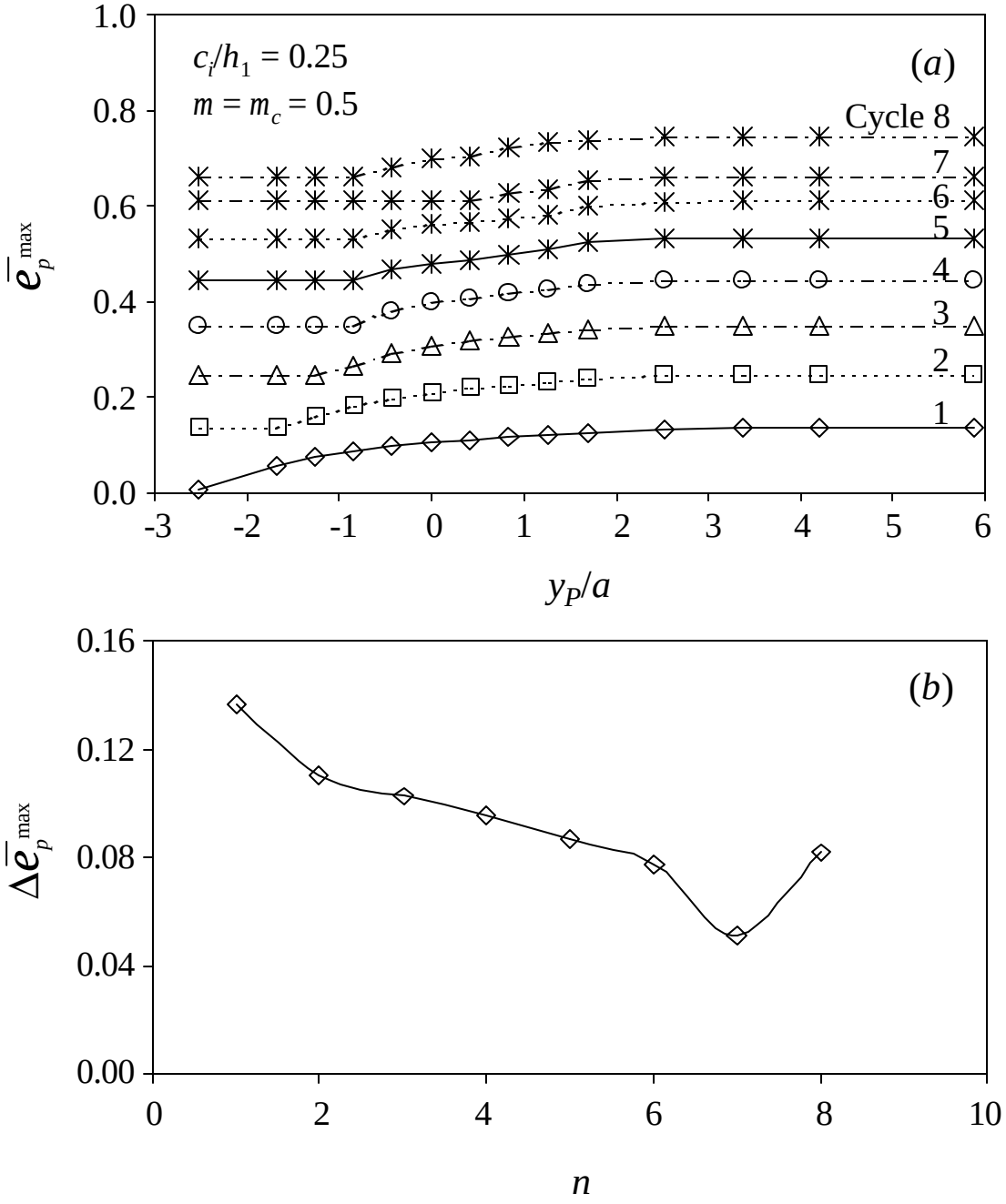
$c_i/h_1 = 0.25$
$m = m_c = 0.5$
(a)
Cycle 8
7
6
5
4
3
2
1
$\bar{e}_p^{\max}$
y_P/a
(b)
$\Delta\bar{e}_p^{\max}$
n

Figure 15